VIP | Carbon | *Very Important Paper*

# Locally Ordered Graphitized Carbon Cathodes for High-Capacity Dual-Ion Batteries

*Kai Yang[+], Qirong Liu[+], Yongping Zheng[+], Hang Yin, Shanqing Zhang,\* and Yongbing Tang\**

***Abstract:*** *Dual-ion batteries (DIBs) inherently suffer from limited energy density. Proposed here is a strategy to effectively tackle this issue by employing locally ordered graphitized carbon (LOGC) cathodes. Quantum mechanical modeling suggests that strong anion–anion repulsions and severe expansion at the deep-charging stage raise the anion intercalation voltage, therefore only part of the theoretical anion storage sites in graphite is accessible. The LOGC interconnected with disordered carbon is predicted to weaken the interlaminar van der Waals interactions, while disordered carbons not only interconnect the dispersed nanographite but also partially buffer severe anion–anion repulsion and offer extra capacitive anion storage sites. As a proof-of-concept, ketjen black (KB) with LOGC was used as a model cathode for a potassium-based DIB (KDIB). The KDIB delivers an unprecedentedly high specific capacity of 232 mAh g⁻¹ at 50 mA g⁻¹, a good rate capability of 110 mAh g⁻¹ at 2000 mA g⁻¹, and excellent cycling stability of 1000 cycles without obvious capacity fading.*

$\mathbf{D}$eveloping cost-effective energy storage systems is pivotally important in the implementation of intermittent renewable energy sources (e.g., solar and wind). Although lithium-ion batteries (LIBs) have been widely used in portable and automotive energy storage systems, the scarcity and uneven distribution of lithium element in Earth's crust limit their large-scale applications.[1] Non-lithium batteries such as sodium-ion batteries (SIBs),[2] potassium-ion batteries (KIBs),[3] and aluminum-ion batteries (AIBs),[4] therefore, have attracted increasing research interests. However, the search for cation-intercalating cathode materials for these non-lithium rocking-chair batteries is challenging due to the larger ionic radius (e.g., $Na^+$ and $K^+$) or higher charge density (e.g., $Mg^{2+}$ and $Ca^{2+}$) of post-lithium cations.[5] Dual-ion batteries (DIBs) are a potential solution to circumventing the difficulty in developing cation-intercalating cathode materials by a distinctive cation-anion dual-carrier chemistry, i.e., cation only shuttling back and forth between anode and electrolyte, while anions ($PF_6^-$, $FSI^-$, $AlCl_4^-$, $TFSI^-$, etc.) reversibly intercalate/de-intercalate into/from cathodes, typically graphite materials.[6] These DIB configurations bring about high working voltages and excellent rate-performance, together with low cost and environmental friendliness.[7]

However, a major hurdle of DIBs is their low energy densities compared with conventional LIBs, stemming from the insufficient specific capacity of anion-intercalating graphite cathodes.[8] A simple theoretical model based on the geometric limit calculation for anion storage in graphite has predicted the theoretical specific capacity of different anions, e.g., 140 mAh g⁻¹ for $C_{16}(PF_6)$, 186 mAh g⁻¹ for $C_{12}(FSI)$.[9] Nevertheless, so far less than 100 mAh g⁻¹ was experimentally reported for DIBs with graphite cathodes, particularly when post-lithium ions (e.g., $K^+$, $Mg^{2+}$, $Ca^{2+}$) are used as the active cations.[6c,10] The underlying physics and chemistry that underpin the discrepancy of the capacity limit between theory and experiment are yet to be elucidated with more sophisticated calculations. Hitherto, an empirical design strategy that using graphite with high graphitization degree and large area of the "non-basal plane" is considered as the effective way to boost the anion storage of graphite.[9a,11] Accordingly, a common practice to reduce the diffusion resistance of anions is to design defect-free and/or few-layer graphite cathodes.[12] Although the strategy enhances the intercalation kinetics of anions to some extent,[12a–d] the practical specific capacity of graphite cathodes for anion storage still remains as a bottleneck. In this regard, it is of great significance to obtain further fundamental insights into the anion storage behavior for the sake of addressing the capacity bottleneck of graphite cathodes.

In this work, we proposed an unconventional design strategy by employing locally ordered graphite carbon (LOGC) interconnected with disordered carbon as the anion-intercalating cathode, in order to overcome the capacity limit of defect-free graphite. Density functional theory (DFT) calculations suggest that the LOGC carbon materials with reduced layer size could effectively weaken the van der Waals interaction between adjacent graphene sheets and thus to reduce the anion-intercalating voltage attributed

[*] K. Yang,[+] Dr. Q. R. Liu,[+] Dr. Y. P. Zheng,[+] H. Yin, Prof. Y. B. Tang
Functional Thin Films Research Center, Shenzhen Institutes of Advanced Technology, Chinese Academy of Sciences
Shenzhen 518055 (China)
E-mail: tangyb@siat.ac.cn

K. Yang,[+] Prof. Y. B. Tang
Nano Science and Technology Institute, University of Science and Technology of China, Suzhou 215123 (China)

Prof. S. Q. Zhang
Center for Clean Environment and Energy School of Environment and Science, Griffith University
Brisbane, Queensland 4222 (Australia)
E-mail: s.zhang@griffith.edu.au

Prof. Y. B. Tang
Key Laboratory of Advanced Materials Processing & Mold, Ministry of Education, Zhengzhou University, Zhengzhou 450002 (China)

Prof. Y. B. Tang
School of Chemical Sciences, Ministry of Education, University of Chinese Academy of Sciences, Beijing 100049 (China)

[+] These authors contributed equally to this work.

Supporting information and the ORCID identification number(s) for the author(s) of this article can be found under:
https://doi.org/10.1002/anie.202016233.

**6326** Wiley Online Library

© 2020 Wiley-VCH GmbH

*Angew. Chem. Int. Ed.* **2021**, 60, 6326–6332

by the graphite expansion; meanwhile, disordered carbons not only interconnect the dispersed nanographite but also partially buffer severe anion-anion repulsion and offer extra capacitive anion storage sites. These merits eventually result in increased anion-storage capacity within the electrolyte electrochemical stability (EES) window. To validate this novel design strategy, commercial ketjen black (KB) with a typical LOGC structure was selected as a proof-of-concept cathode material for a potassium-based DIB (KDIB), while fully disordered activated carbon (AC) and fully ordered graphite were selected as the controlled cathodes. As predicted, the KDIB with KB cathode delivers an unprecedentedly high specific capacity of 232 mAh g$^{-1}$ at 50 mA g$^{-1}$ which is significantly improved in comparison with the controlled samples (e.g., the commercial natural graphite and AC), and excellent cycling stability up to 1000 cycles without obvious capacity fading at 300 mA g$^{-1}$, outperforming both controlled cathodes. This work will inspire further studies on LOGC carbon materials for developing high-capacity anion-storage cathode in DIBs.

Firstly, we apply first-principles DFT calculations to reveal the fundamental principles that underpin the capacity limit for anion storage in graphite cathode. As shown in Figure 1a, the formation energies of $C_{16}(PF_6)_x$ ($x = 0$, 0.125, 0.25, 0.33, 0.5, 0.57, 0.67, 0.8, 1) phases are calculated with respect to the free energies of graphite (i.e., $x = 0$) and $C_{16}PF_6$ (i.e., $x = 1$). For the calculations, we search the global minimum of each phase by enumerating the anion intercalation stage, anion arrangement, and initial graphite layer distance. Therefore, the blue dots on the convex hull represent the most stable anion intercalation configurations

at each $PF_6^-$ content $x$, a species produced during the charge-discharge process. At $x \leq 0.5$, we find at least three two-phase reactions upon anion intercalation into graphite, where the anion arrangement goes from stage VIII to IV to II. At $x = 0.33$, the formation energy of stage III is slightly above the convex hull, indicating a decomposition reaction into stage IV and II. While at $0.5 \leq x \leq 0.8$, solid-solution reactions take place within stage II, until the final two-phase reaction between stage II and I at $0.8 \leq x \leq 1$. Figure 1b shows the voltage profile corresponding to the phase reactions calculated in Figure 1a, which implies that only $\approx 70$ mAh g$^{-1}$, half of the geometrically limited anion storage capacity in graphite, is accessible because the voltage raises ($> 5.5$ V versus K$^+$/K) beyond the EES window at $x \geq 0.5$. This calculated capacity limit is consistent with the previously reported experimental result that the KPF$_6$ based KDIB only showed a discharge capacity of below 50 mAh g$^{-1}$,[13] which indicates the success of our calculation model in predicting the anion storage behavior.

Figure S1 (see the Supporting Information) displays the graphite layer buckling upon initial anion intercalation due to the large size of $PF_6^-$ and van der Waals interaction between graphite layers. Such the buckling effect is in line with the reported results, where some tortile lattice fringes are observed from the anion-intercalated graphite cathode.[14] Van der Waals forces between large-sized graphite layers exert high energy barriers on anion intercalation (Figure S2), and raise the anion intercalation voltage. Therefore, a small size down to 2 nm (LOGC structure) may effectively reduce the diffusion energy barrier of anions and mitigate the over-high voltage at the deep charging stage. Besides, abundant edges of these small-sized carbonaceous slices allow extra anion adsorption and greatly increase the specific capacity.[12e] As expected, DFT calculations in Figure 1c shows that carbon materials like KB with LOGC structure can achieve an anion-intercalation capacity of 127.6 mAh g$^{-1}$ within the EES window ($< 5$ V vs. K$^+$/K). The $PF_6^-$ storage in interlayer and edge sites of nanographite is conducive to alleviating the severe anion repulsion and thus to reducing the anion storage voltage. For comparison, we also consider the fully disordered carbon such as AC. Although with a large specific surface area, the calculated anion storage capacity (Figure 1c) within the EES window is only 63.8 mAh g$^{-1}$, presumably because the fully open structure without layered intercalation results in under-coordinated anions and over-high storage voltage. This predicted insufficient capability for anion storage in fully disordered carbon (such as AC) is in line with the reported low specific capacity of KDIBs based on AC cathodes.[6b, 8c, 15] Figure 1d summarizes the schematic voltage variation along with graphitization degree, which implies that the optimum graphitization degree should be "just right", i.e., neither too high nor too low, to effectively mitigate the over-high voltage of anion storage in carbon materials.

To further experimentally explore the feasibility of LOGC structured design strategy of carbon cathode for KDIBs, three typical carbon structures of disordered carbon (i.e., AC, Figure 2a), fully graphitized carbon (i.e., graphite, Figure 2d), and LOGC carbon (i.e., KB, Figure 2g) are exploited as the proof-of-concept cathodes. The DFT calculations
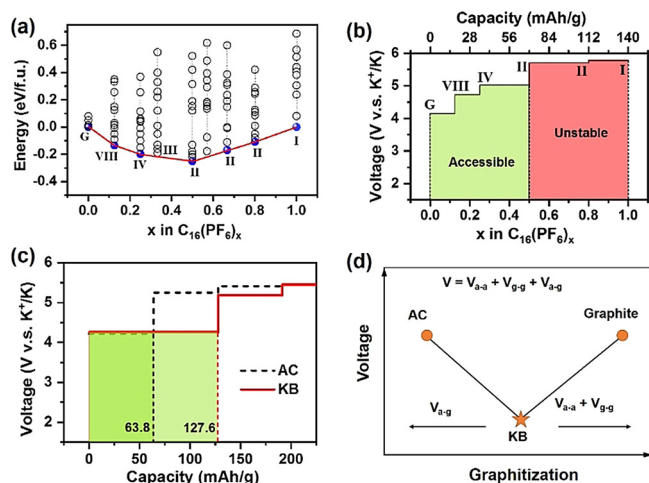


***Figure 1.*** DFT calculations of anion storage behavior in different types of carbon. a) Formation energy of $C_{16}(PF_6)_x$ as a function of $PF_6^-$ content $x$ in graphite. The blue dots represent the most stable configurations at each $PF_6^-$ insertion stage, and the red line is the convex hull of the formation energy. b) Calculated voltage profile as a function of $PF_6^-$ content $x$ in graphite and the corresponding specific capacity. c) Calculated voltage profiles versus $PF_6^-$ storage capacity in AC and KB. d) Schematic voltage evolution of anion storage in carbons as a function of graphitization degree. $V_{a-a}$, $V_{g-g}$, and $V_{a-g}$ are the voltage contributed by anion-anion, graphene-graphene, and anion-graphene interactions, respectively.
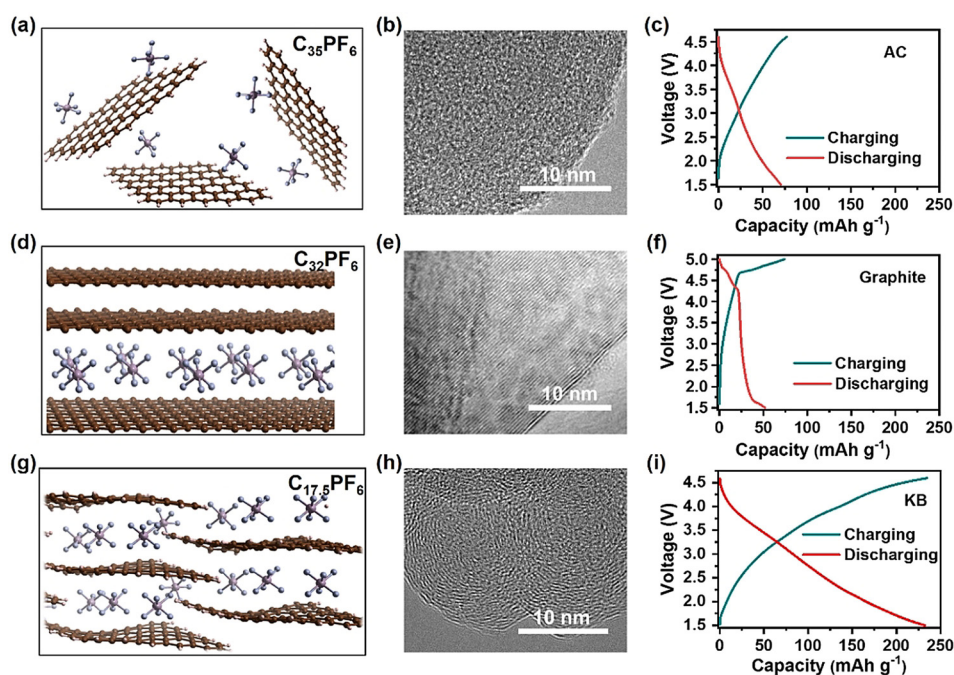
**Figure 2.** Comparison between three typical carbon cathodes with different microstructures. Schematic anion storage mechanisms of disordered carbon (a), fully graphitized carbon (d), and LOGC (g), and HRTEM images of AC (b), graphite (e), and KB (h) and their individually typical galvanostatic charge-discharge curves (c,f,i).

suggest that the anion storage at the disordered carbon cathode mainly occurs at the edges of carbon nanosheets with an average stage of $C_{35}PF_6$ (Figure 2a), induced by an anion adsorption behavior. Figure 2b shows a typical high-resolution transmission electron microscope (HRTEM) image of the AC material. There is no presence of crystalline phases, confirming the amorphous and disordered nature of AC, in agreement with Figure 2a. A further experimental result in Figure 2c presents that the AC cathode delivers a discharge specific capacity of less than 70 mAh g$^{-1}$, consistent with the theoretical calculations. Furthermore, the DFT calculation indicates that, in the case of fully graphited carbon cathode, the anion intercalation into adjacent graphene interlayers enables the anion storage with stage 2, corresponding to the formula of $C_{32}PF_6$ (Figure 2d). The typical example is graphite materials, their physical structure is dominated by crystalline domains (Figure 2e). The anion storage capability can be also confirmed by an experimental measurement (Figure 2f), where only a discharge capacity of about 50 mAh g$^{-1}$ is obtained. The initial experimental capacities of the AC and graphite cathode in KDIBs are consistent with the reported results.[6b,13,15,16] In contrast, the LOGC carbon cathode theoretically endows with a synergistic anion storage mechanism of intercalation and adsorption (Figure 2g). Taking the KB for instance, it clearly presents some LOGC features with an interlayer spacing of about 0.356 nm (Figure 2h and Figure S3). More detailed physical and chemical information of KB is provided in Figures S4–S6. The DFT calculations show that the specific capacity of anion intercalation drastically increases to 127.6 mAh g$^{-1}$ corresponding to $C_{17.5}PF_6$ (Figure 2g), owing to the weakened van der Waals interaction between adjacent graphene layers. Besides, a large

specific surface area bestows the KB cathode with an enhanced ability to allow extra anion adsorption, and thus to improve the capacitive capacity of the carbon cathode. As observed, neither ideal straight lines nor obvious voltage plateau are presented for both charge and discharge profiles. Such behavior implies that the electrochemical energy-storage process is controlled by the synergistic anion storage mechanism of diffusion behavior and capacitive characteristic.[8c] After an activation procedure, the KDIB delivers a stable specific capacity of over 232 mAh g$^{-1}$ at a current density of 50 mA g$^{-1}$ (Figure 2i and Figure S7), which is the highest value for cathode materials in KDIBs so far. Correspondingly, a high coulombic efficiency of ca. 99% is obtained for the half-cell at the 100$^{th}$ cycle. The comparative analyses of three carbon cathodes validate the feasibility of this novel design strategy.

To further clarify the electrochemical working mechanism of KB, X-ray photoelectron spectroscopy (XPS), Fourier transform infrared (FTIR) spectroscopy, Raman spectra, and TEM were applied to characterize the chemical composition and physical properties. As shown in Figure 3a, remarkably strong signal intensity can be observed in the high-resolution P 2p XPS spectrum of the fully charged KB cathode. In contrast, at the fully discharged state, the signal intensity becomes much weaker, which implies the reversible adsorption/intercalation of $PF_6^-$ anions onto/into the KB cathode during the charging process. In Figure 3b, the FTIR spectra of KB cathode at pristine, fully charged, and fully discharged states provide further evidence for the anionic adsorption/intercalation mechanism. As observed, for the fully charged KB, FTIR shows a remarkable absorption peak in the wavenumber range of 820–850 cm$^{-1}$, assigned to the P-F stretching vibration of the octahedral $PF_6^-$, which is in association with the adsorption/intercalation of $PF_6^-$ anions during the charging process.[4a,17] In the case of the fully discharged state, there is a distinctly weakened peak in the same wavenumber range, signifying the desorption/de-intercalation of $PF_6^-$ anions in the discharging process. The weak signal intensity may be attributed to residual electrolyte salt and/or partial irreversibility of the adsorbed/intercalated $PF_6^-$ anions. Raman spectra of KB cathode at different charged/discharged states were acquired to analyze its electrochemical anion-storage process. As shown in Figure 3c, two characteristic peaks of carbon at 1342 cm$^{-1}$ and 1588 cm$^{-1}$ denoting D band and G band can be observed, which individually relate to the disordred/defective carbon and ordered/graphitized
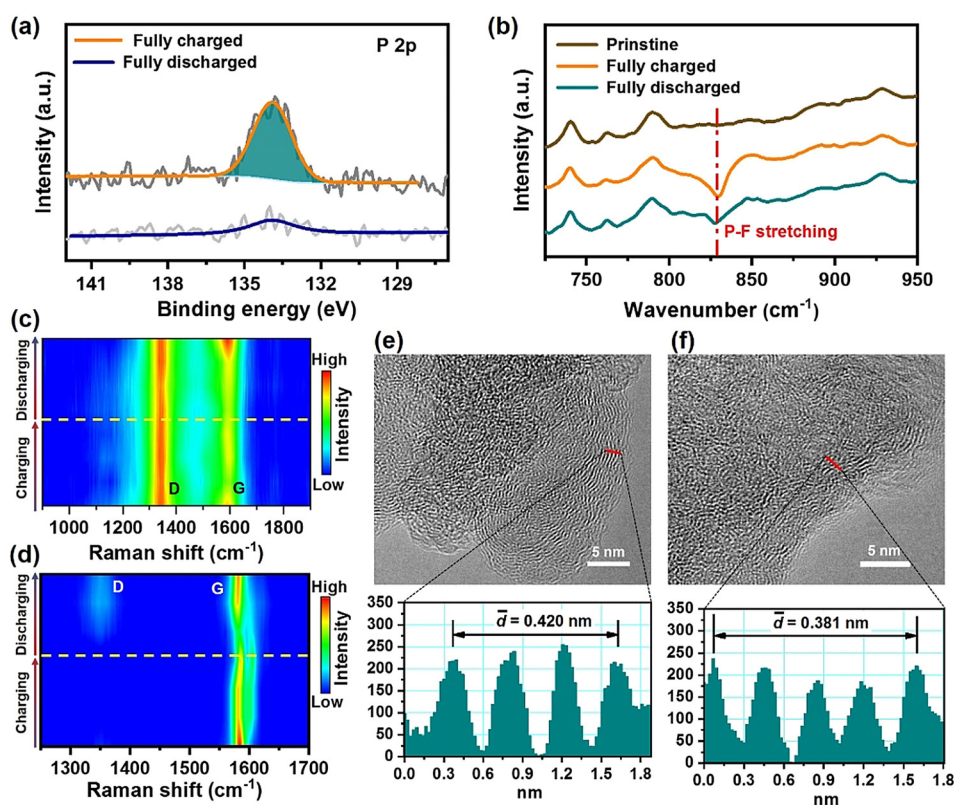
***Figure 3.*** Working mechanism studies of KB cathode in the KDIB. a) High-resolution P 2p XPS spectra in the KB cathode at fully charged and discharged states; b) FTIR spectra of KB cathode at pristine, fully charged and discharged states; Raman spectra of c) KB and d) graphite cathodes during charging-discharging processes; and e,f) HRTEM images and corresponding interlayer spacing of KB carbon cathode at fully charged (d) and discharged (e) states.

carbon. As the charging process goes on, the relative intensity of G band decreases, indicating the anion storage further disarranges the LOGC structure of KB cathode. However, there is no presence of obvious peak shift, implying that no obvious mechanical stress/strain is generated during the anion storage process. During the subsequent discharging process, the relative intensity is recoverable, which suggests excellent anion-storage reversibility of KB cathode. In the case of graphite cathode (Figure 3 d), the anion intercalation during the charging process brings about a weakening peak intensity, accompanied by peak shift, and even the emergence of new peak of G band. Although the discharging process leads to a reverse change of G band, the weak characteristic peak of D band can be observed at the end of discharging process. Such evolution of Raman spectra indicates the anion intercalation into graphite cathode leads to large stress/strain,[18] because the anion intercalation process has to conquer the van der Waals interaction inside graphite, and inevitably cause the structure change of graphite cathode. The anion intercalation/ de-intercalation behavior also partially damages the graphite structure. The comparative study implies that the design strategy of LOGC is conducive to weakening the van der Waals interaction and to improving structural stability of cathode in DIBs. HRTEM images suggest that, compared with the pristine sample (ca. 3.56 Å, Figure S3), the fully charged KB presents an increased interlayer spacing (ca. 4.20 Å, Figure 3 e). By contrast, the discharging process gives

rise to a decreased interlayer spacing (ca. 3.81 Å, Figure 3 f). Such evolution is consistent with the previously reported results of anion-intercalated graphite cathode,[14] which further authenticates the occurrence of anionic reversible intercalation/de-intercalation behaviors during galvanostatic charging/discharging processes.

In order to get further insight into the electrochemical energy-storage behavior, the kinetic process of KB cathode is investigated on the basis of cyclic voltammetry (CV) profiles at scan rates of 0.4 to 1.2 mV s$^{-1}$ in a voltage range from 1.5 V to 4.6 V (vs. K/K$^+$). As shown in Figure 4a, no typical rectangle shapes are presented for these CV curves, and relatively weak redox peaks can be observed, signifying the synergistic existence of diffusion behavior and capacitive characteristics. The synergistic effect of electrochemical kinetic process can also be quantitatively analyzed, according to the power-law relationship between peak current, *i*, and scan rate, *v*, as following:[19]

$$i = a v^b \qquad (1)$$

Where *a* and *b* are adjustable constants. The value of *b* locates between 0.5 and 1.0, the former represents diffusion-controlled behavior for electrochemical reaction, and the latter denotes capacitive characteristic of the energy-storage process. In this work, the *b* value is 0.76 (Figure 4b), implying a comparable contribution of diffusion behavior with that of
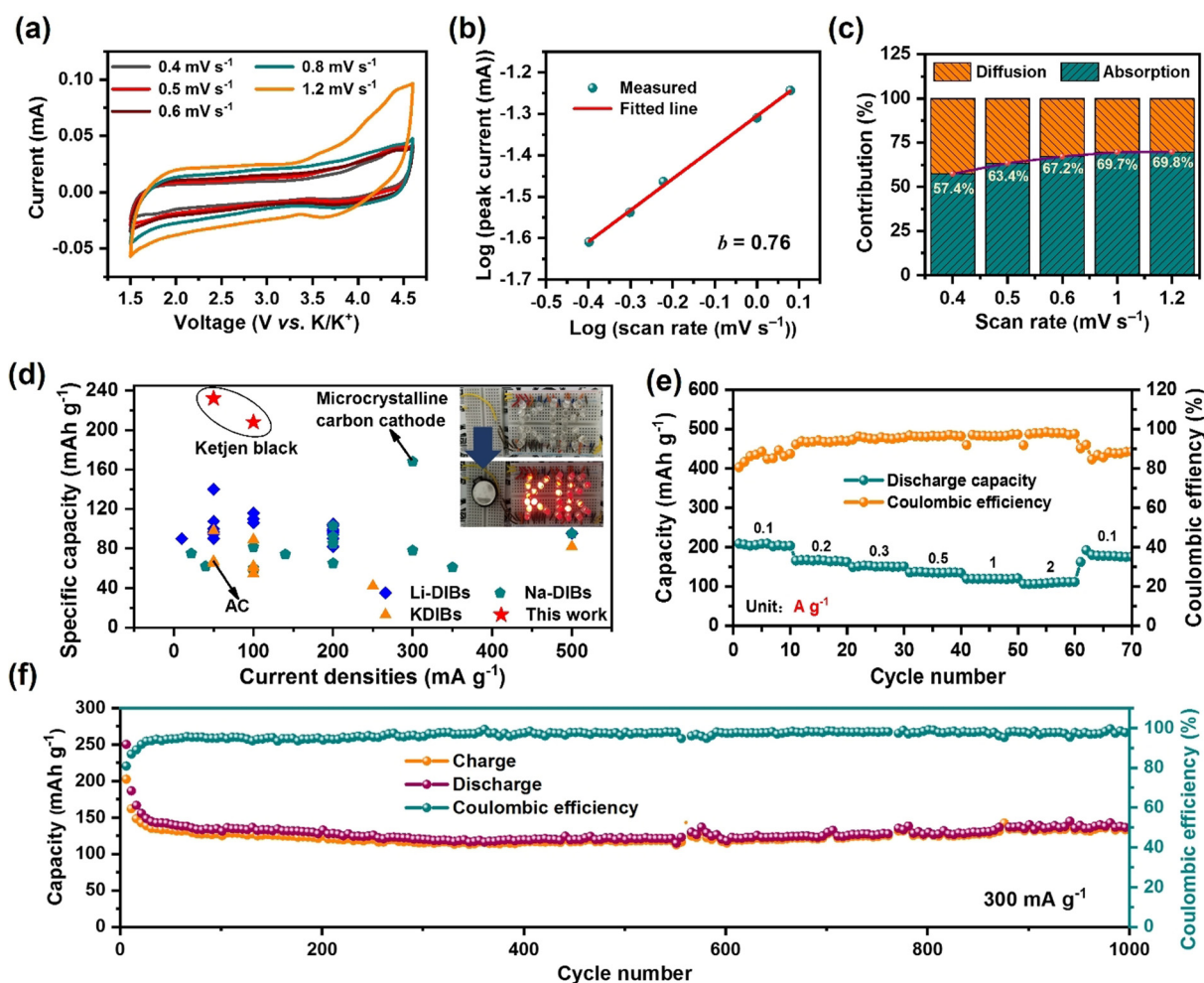
**Figure 4.** Kinetic analyses and electrochemical performances of KB cathode in a KDIB. a) CV profiles of the KB cathode in a KDIB at different scan rates from 0.4 to 1.2 mV s$^{-1}$, and b) corresponding *b* value deriving from the relationship of Equation (2). c) Contribution fraction of the capacitive behavior to the capacities at different scan rates. d) Comparison of specific capacity of the KB-based KDIB with other previously reported DIBs based on carbon cathodes. Inset is optical photographs of thirty LEDs in parallel before and after lighted up by a fully charged KDIB. e) Rate capability and f) long-term cycling performance of the KDIB.

the capacitive process. As presented in Figure 4c, the capacitive process contributes to 57.4% of the total charge storage at the scan rate of 0.4 mV s$^{-1}$, indicating that a comparable capacity contribution at low rates stems from the diffusion behavior of anion intercalation into carbon interlayers. Accompanying with the increasing scan rate, the capacitive contribution fraction gradually increases to 69.8% at 1.2 mV s$^{-1}$ (Figure S8). The large capacitive contribution can be attributed to the large specific surface area of KB, which provides more facile accessibility for anion adsorption with fast kinetics. In contrast, the diffusion behavior in the KB cathode is limited by the relatively slow intercalation kinetics of anions into the carbon layers with the LOGC structure at high current densities.

The kinetics of KB cathode is further analyzed with electrochemical impedance spectroscopy (EIS) in a frequency range of 1 MHz to 0.01 Hz. As shown in Figure S9, in the Nyquist plots of the half-cell after different cycles, there are almost the same intercept on the real axis at high frequency, signifying stably internal resistance of the electrode material.

The semicircular curves in the medium-frequency region involve charge transfer resistance ($R_{ct}$). Obviously, even though a slight increasing $R_{ct}$ can be observed in early cycles, $R_{ct}$ tends to be a stable value after 120 cycles, indicating the formation of a stable SEI layer and good cycling stability of KB cathode.

The electrochemical energy storage properties of the KDIB based on KB cathode were further evaluated to validate the feasibility of the LOGC design strategy. As shown in Figure 4d, the KDIB shows great superiorities of specific capacity over previously reported lithium-based DIBs (Li-DIBs),[20] sodium-based DIBs (Na-DIBs)[6a,8a,21] and KDIBs.[3a,6b,9a,10a,16,22] The high specific capacity of microcrystalline carbon cathode[8a] provided extra evidence for the novel design strategy in this work. As a result, such a battery can light up thirty LEDs with red color (around 1.8–2.2 V) in parallel. Also, the specific capacity of the KDIBs also surpasses that of other typical cathode materials for KIBs (Figure S10), including different types of layered transition-metal oxides,[23] Prussian blue analogues,[24] polyanionic com-

pounds,[25] organics,[26] etc. Moreover, the rate capability and the cycling stability of KB cathode are also evaluated. As shown in Figure 4e, the discharge capacities of 208, 167, 152, 136, 119 and 110 mAh g$^{-1}$ are retained for the half-cell at 100, 200, 300, 500, 1000, and 2000 mA g$^{-1}$, respectively. As shown in Figure S11, such a rate capability is clearly superior to that of other reported KDIBs or hybrid potassium-based energy-storage devices.[7c,9a,10a,17d,21a,22a,27] Meantime, the reversible capacity is recoverable as the current density returns to 100 mA g$^{-1}$, which demonstrates an outstanding rate capability of KB cathode, ascribable to its low energy barrier of anion intercalation/de-intercalation into/from LOGC carbon cathode, large specific surface area and excellent electronic conductivity. Expectably, the KDIB also shows excellent cycling stability of 1000 cycles without capacity fading at 300 mA g$^{-1}$ (Figure 4 f).

In summary, according to the theoretical DFT calculation, the low specific capacity of graphite cathode in DIBs was mainly caused by the high energy barrier of anion diffusion, and experimentally, we proposed a locally ordered graphited carbon (LOGC) structure for carbon cathodes to enhance the anionic diffusion kinetics and lower the corresponding diffusion potential. A commercial ketjen black (KB) was chosen as a proof-of-concept cathode material for robust, high-capacity KDIBs, since its LOGC structure and large specific surface area can afford densely distributed accessible active sites with weakened interlayered van der Waals interaction for facilating anion intercalation, and additionally available sites for anion adsorption. As expected, the KB cathode exhibited an ultrahigh specific capacity up to 232 mAh g$^{-1}$ at 50 mA g$^{-1}$, the highest value among reported DIBs, and a superior rate capability of 110 mAh g$^{-1}$ at 2000 mA g$^{-1}$. Besides, the LOGC characteristic and unique branched-chain structure generated outstanding cycling stability without obvious capability decay after 1000 cycles at 300 mA g$^{-1}$. Although the structural design of LOGC cathodes could be further improved via optimization of the entire electrochemical system, this work could shed light on developing high-performance cathode materials for DIBs.

## Acknowledgements

## Conflict of interest

The authors declare no conflict of interest.

[1] a) J. Chen, B. Yang, H. Li, P. Ma, J. Lang, X. Yan, *J. Mater. Chem. A* **2019**, *7*, 9247–9252; b) X. Zhao, Y. Tang, C. Ni, J. Wang, A. Star, Y. Xu, *ACS Appl. Energy Mater.* **2018**, *1*, 1703–1707; c) G. Wang, X. Xiong, D. Xie, Z. Lin, J. Zheng, F. Zheng, Y. Li, Y. Liu, C. Yang, M. Liu, *J. Mater. Chem. A* **2018**, *6*, 24317–24323.

[2] a) N. Yabuuchi, K. Kubota, M. Dahbi, S. Komaba, *Chem. Rev.* **2014**, *114*, 11636–11682; b) W. Wang, Y. Gang, Z. Hu, Z. Yan, W. Li, Y. Li, Q. F. Gu, Z. Wang, S. L. Chou, H. K. Liu, S. X. Dou, *Nat. Commun.* **2020**, *11*, 980; c) Y. Wang, L. Wang, H. Zhu, J. Chu, Y. Fang, L. Wu, L. Huang, Y. Ren, C.-J. Sun, Q. Liu, X. Ai, H. Yang, Y. Cao, *Adv. Funct. Mater.* **2020**, *30*, 1910327; d) D. Yang, W. Chen, X. Zhang, L. Mi, C. Liu, L. Chen, X. Guan, Y. Cao, C. Shen, *J. Mater. Chem. A* **2019**, *7*, 19709–19718.

[3] a) K. Beltrop, S. Beuker, A. Heckmann, M. Winter, T. Placke, *Energy Environ. Sci.* **2017**, *10*, 2090–2094; b) W. Zhang, W. K. Pang, V. Sencadas, Z. Guo, *Joule* **2018**, *2*, 1534–1547; c) Q. Pan, D. Gong, Y. B. Tang, *Energy Storage Mater.* **2020**, *31*, 328–343; d) B. Ji, W. Yao, Y. Zheng, P. Kidkhunthod, X. Zhou, S. Tunmee, S. Sattayaporn, H.-M. Cheng, H. He, Y. B. Tang, *Nat. Commun.* **2020**, *11*, 1225; e) H. He, W. Yao, S. Tunmee, X. Zhou, B. Ji, N. Wu, T. Song, P. Kidkhunthod, Y. B. Tang, *J. Mater. Chem. A* **2020**, *8*, 9128–9136.

[4] a) M. L. Aubrey, J. R. Long, *J. Am. Chem. Soc.* **2015**, *137*, 13594–13602; b) T. Placke, A. Heckmann, R. Schmuch, P. Meister, K. Beltrop, M. Winter, *Joule* **2018**, *2*, 2528–2550; c) E. Zhang, B. Wang, J. Wang, H. Ding, S. Zhang, H. Duan, X. Yu, B. Lu, *Chem. Eng. J.* **2020**, *389*, 124407.

[5] a) W. Wang, J. Zhou, Z. Wang, L. Zhao, P. Li, Y. Yang, C. Yang, H. Huang, S. Guo, *Adv. Energy Mater.* **2018**, *8*, 1701648; b) T. Masese, K. Yoshii, Y. Yamaguchi, T. Okumura, Z. D. Huang, M. Kato, K. Kubota, J. Furutani, Y. Orikasa, H. Senoh, H. Sakaebe, M. Shikano, *Nat. Commun.* **2018**, *9*, 3823; c) L. G. Xue, Y. T. Li, H. C. Gao, W. D. Zhou, X. J. Lu, W. Kaveevivitchai, A. Manthiram, J. B. Goodenough, *J. Am. Chem. Soc.* **2017**, *139*, 2164–2167; d) G. Li, B. Huang, Z. Pan, X. Su, Z. Shao, L. An, *Energy Environ. Sci.* **2019**, *12*, 2030–2053; e) B. Ji, H. He, W. Yao, Y. B. Tang, *Adv. Mater.* **2020**, *32*, 2005501; f) Y. Lan, W. Yao, X. He, T. Song, Y. Tang, *Angew. Chem. Int. Ed.* **2020**, *59*, 9255; *Angew. Chem.* **2020**, *132*, 9342.

[6] a) Y. J. Liu, X. Hu, G. B. Zhong, J. X. Chen, H. B. Zhan, Z. H. Wen, *J. Mater. Chem. A* **2019**, *7*, 24271–24280; b) L. Fan, K. R. Lin, J. Wang, R. F. Ma, B. G. Lu, *Adv. Mater.* **2018**, *30*, 1800804; c) M. Wang, C. L. Jiang, S. Q. Zhang, X. H. Song, Y. B. Tang, H. M. Cheng, *Nat. Chem.* **2018**, *10*, 667–672; d) Q. Liu, H. Wang, C. Jiang, Y. Tang, *Energy Storage Mater.* **2019**, *23*, 566–586; e) Y. Feng, S. Chen, J. Wang, B. Lu, *J. Energy Chem.* **2020**, *43*, 129–138.

[7] a) X. Zhou, Q. Liu, C. Jiang, B. Ji, X. Ji, Y. Tang, H.-M. Cheng, *Angew. Chem. Int. Ed.* **2020**, *59*, 3802–3832; *Angew. Chem.* **2020**, *132*, 3830–3861; b) X. Ding, F. Zhang, B. Ji, Y. Liu, J. Li, C.-S. Lee, Y. Tang, *ACS Appl. Mater. Interfaces* **2018**, *10*, 42294–42300; c) L. Fan, Q. Liu, Z. Xu, B. G. Lu, *ACS Energy Lett.* **2017**, *2*, 1614–1620; d) X. Jiang, L. Luo, F. Zhong, X. Feng, W. Chen, X. Ai, H. Yang, Y. Cao, *ChemElectroChem* **2019**, *6*, 2615.

[8] a) G. Zhang, X. Ou, C. Cui, J. Ma, J. Yang, Y. B. Tang, *Adv. Funct. Mater.* **2019**, *29*, 1806722; b) X. Qi, K. Huang, X. Wu, W. Zhao, H. Wang, Q. Zhuang, Z. Ju, *Carbon* **2018**, *131*, 79–85; c) N. Wu, W. Yao, X. Song, G. Zhang, B. Chen, J. Yang, Y. B. Tang, *Adv. Energy Mater.* **2019**, *9*, 1803865; d) H. Lei, J. Tu, Z. Yu, S. Jiao, *ACS Appl. Mater. Interfaces* **2017**, *9*, 36702–36707.

[9] a) K. V. Kravchyk, P. Bhauriyal, L. Piveteau, C. P. Guntlin, B. Pathak, M. V. Kovalenko, *Nat. Commun.* **2018**, *9*, 4469; b) C. Yang, J. Chen, X. Ji, T. P. Pollard, X. Lü, C.-J. Sun, S. Hou, Q.

Liu, C. Liu, T. Qing, Y. Wang, O. Borodin, Y. Ren, K. Xu, C. Wang, *Nature* **2019**, *569*, 245–250.

[10] a) N. Li, F. Zhang, Y. B. Tang, *J. Mater. Chem. A* **2018**, *6*, 17889–17895; b) S. Wu, F. Zhang, Y. B. Tang, *Adv. Sci.* **2018**, *5*, 1701082; c) X. Lei, Y. P. Zheng, F. Zhang, Y. Wang, Y. B. Tang, *Energy Storage Mater.* **2020**, *30*, 34–41.

[11] T. Ishihara, M. Koga, H. Matsumoto, M. Yoshio, *Electrochem. Solid-State Lett.* **2007**, *10*, A74.

[12] a) H. Chen, F. Guo, Y. Liu, T. Huang, B. Zheng, N. Ananth, Z. Xu, W. Gao, C. Gao, *Adv. Mater.* **2017**, *29*, 1605958; b) S. C. Jung, Y.-J. Kang, D.-J. Yoo, J. W. Choi, Y.-K. Han, *J. Phys. Chem. C* **2016**, *120*, 13384–13389; c) L. Zhang, L. Chen, H. Luo, X. Zhou, Z. Liu, *Adv. Energy Mater.* **2017**, *7*, 1700034; d) H. Chen, H. Xu, S. Wang, T. Huang, J. Xi, S. Cai, F. Guo, Z. Xu, W. Gao, C. Gao, *Sci. Adv.* **2017**, *3*, eaao7233; e) Q. Zhang, L. Wang, J. Wang, C. Xing, J. Ge, L. Fan, Z. Liu, X. Lu, M. Wu, X. Yu, H. Zhang, B. Lu, *Energy Storage Mater.* **2018**, *15*, 361–367.

[13] M. Zhang, M. Shoaib, H. Fei, T. Wang, J. Zhong, L. Fan, L. Wang, H. Luo, S. Tan, Y. Wang, J. Zhu, J. Hu, B. Lu, *Adv. Energy Mater.* **2019**, *9*, 1901663.

[14] a) Q. Liu, G. Zhang, N. Chen, X. Feng, C. Wang, J. Wang, X. Jin, L. Qu, *Adv. Funct. Mater.* **2020**, *30*, 2002086; b) S. Wang, S. Jiao, D. Tian, H. S. Chen, H. Jiao, J. Tu, Y. Liu, D. N. Fang, *Adv. Mater.* **2017**, *29*, 1606349.

[15] Z. Zhang, M. Li, Y. Gao, Z. Wei, M. Zhang, C. Wang, Y. Zeng, B. Zou, G. Chen, F. Du, *Adv. Funct. Mater.* **2018**, *28*, 1802684.

[16] B. Ji, F. Zhang, X. Song, Y. Tang, *Adv. Mater.* **2017**, *29*, 1700519.

[17] a) K. S. Mohamed, D. K. Padma, *Spectrochim. Acta Part A* **1985**, *41A*, 725–728; b) C. Han, R. Shi, D. Zhou, H. Li, L. Xu, T. Zhang, J. Li, F. Kang, G. Wang, B. Li, *ACS Appl. Mater. Interfaces* **2019**, *11*, 15646–15655; c) J. Syzdek, M. Marcinek, R. Kostecki, *J. Power Sources* **2014**, *245*, 739–744; d) C. Li, J. Xue, A. Huang, J. Ma, F. Qing, A. Zhou, Z. Wang, Y. Wang, J. Li, *Electrochim. Acta* **2019**, *297*, 850–855.

[18] I. A. Kinloch, J. Suhr, J. Lou, R. J. Young, P. M. Ajayan, *Science* **2018**, *362*, 547–553.

[19] a) P. Lu, Y. Sun, H. Xiang, X. Liang, Y. Yu, *Adv. Energy Mater.* **2018**, *8*, 1702434; b) Y. Xu, C. L. Zhang, M. Zhou, Q. Fu, C. X. Zhao, M. H. Wu, Y. Lei, *Nat. Commun.* **2018**, *9*, 1720.

[20] a) G. H. Chen, F. Zhang, Z. M. Zhou, J. R. Li, Y. B. Tang, *Adv. Energy Mater.* **2018**, *8*, 1801219; b) X. Han, G. Xu, Z. Zhang, X. Du, P. Han, X. Zhou, G. Cui, L. Chen, *Adv. Energy Mater.* **2019**, *9*, 1804022; c) C. L. Jiang, Y. Fang, J. H. Lang, Y. B. Tang, *Adv. Energy Mater.* **2017**, *7*, 1700913; d) X. Tong, F. Zhang, G. Chen, X. Liu, L. Gu, Y. Tang, *Adv. Energy Mater.* **2018**, *8*, 1701967; e) Z. Zhou, N. Li, Y. Yang, H. Chen, S. Jiao, W.-L. Song, D. Fang, *Adv. Energy Mater.* **2018**, *8*, 1801439; f) S. Zhang, M. Wang, Z. Zhou, Y. Tang, *Adv. Funct. Mater.* **2017**, *27*, 1703035; g) C. L. Jiang, L. Xiang, S. J. Miao, L. Shi, D. H. Xie, J. X. Yan, Z. J. Zheng, X. M. Zhang, Y. B. Tang, *Adv. Mater.* **2020**, *32*, 1908470; h) P. Qin, M. Wang, N. Li, H. Zhu, X. Ding, Y. Tang, *Adv. Mater.* **2017**, *29*, 1606805; i) X. Tong, F. Zhang, B. Ji, M. Sheng, Y. Tang, *Adv. Mater.* **2016**, *28*, 9979–9985; j) G. Wang, M. Yu, J. Wang, D. Li, D. Tan, M. Löffler, X. Zhuang, K. Müllen, X. Feng, *Adv. Mater.* **2018**, *30*, 1800533; k) F. Zhang, B. Ji, X. Tong, M. Sheng, X. Zhang, C.-S. Lee, Y. Tang, *Adv. Mater. Interfaces* **2016**, *3*, 1600605; l) L. Xiang, X. Ou, X. Wang, Z. Zhou, X. Li, Y. Tang, *Angew. Chem. Int. Ed.* **2020**, *59*, 17924; m) C. Y. Chan, P.-K. Lee, Z. Xu, D. Y. W. Yu, *Electrochim. Acta* **2018**, *263*, 34–39; n) A. Heckmann, J. Thienenkamp, K. Beltrop, M. Winter, G. Brunklaus, T. Placke, *Electrochim. Acta* **2018**, *260*, 514–525; o) J. A. Read, A. V. Cresce, M. H. Ervin, K. Xu, *Energy Environ. Sci.* **2014**, *7*, 617–620; p) X. Han, H. Zhang, T. Liu, X. Du, G. Xu, P. Han, X. Zhou, G. Cui, *J. Mater. Chem. A* **2020**, *8*, 1451–1456; q) K. Shin, F. Zhang, X. Ou, N. Wu, C.-S. Lee, Y. Tang, *J. Mater. Chem. A* **2019**, *7*, 10930–10935; r) S. Wang, X. Xiao, C. Fu, J. Tu, Y. Tan, S. Jiao, *J. Mater. Chem. A* **2018**, *6*, 4313–4323; s) P. Han, X. Han, J. Yao, L. Yue, J. Zhao, X. Zhou, G. Cui, *J. Power Sources* **2018**, *393*, 145–151; t) T. Liu, X. Han, Z. Zhang, Z. Chen, P. Wang, P. Han, N. Ding, G. Cui, *J. Power Sources* **2019**, *437*, 226942.

[21] a) M. Sheng, F. Zhang, B. Ji, X. Tong, Y. Tang, *Adv. Energy Mater.* **2017**, *7*, 1601963; b) Z. Hu, Q. Liu, K. Zhang, L. Zhou, L. Li, M. Chen, Z. Tao, Y.-M. Kang, L. Mai, S.-L. Chou, J. Chen, S.-X. Dou, *ACS Appl. Mater. Interfaces* **2018**, *10*, 35978–35983; c) L. Fan, Q. Liu, S. Chen, Z. Xu, B. Lu, *Adv. Energy Mater.* **2017**, *7*, 1602778; d) H. Zhu, F. Zhang, J. Li, Y. Tang, *Small* **2018**, *14*, 1703951; e) J. Fan, Y. Fang, Q. Xiao, R. Huang, L. Li, W. Yuan, *Energy Technol.* **2019**, *7*, 1800978; f) H.-J. Liao, Y.-M. Chen, Y.-T. Kao, J.-Y. An, Y.-H. Lai, D.-Y. Wang, *J. Phys. Chem. C* **2017**, *121*, 24463–24469; g) D. Xie, M. Zhang, Y. Wu, L. Xiang, Y. Tang, *Adv. Funct. Mater.* **2020**, *30*, 1906770; h) R. Ma, L. Fan, S. Chen, Z. Wei, Y. Yang, H. Yang, Y. Qin, B. Lu, *ACS Appl. Mater. Interfaces* **2018**, *10*, 15751–15759; i) S. Mu, Q. Liu, P. Kidkhunthod, X. Zhou, W. Wang, Y. Tang, *Natl. Sci. Rev.* **2020**, https://doi.org/10.1093/nsr/nwaa178; j) X. Yao, Y. Ke, W. Ren, X. Wang, F. Xiong, W. Yang, M. Qin, Q. Li, L. Mai, *Adv. Energy Mater.* **2019**, *9*, 1803260; k) X. Wang, C. Zheng, L. Qi, H. Wang, *Global Challenges* **2017**, *1*, 1700055.

[22] a) B. Ji, F. Zhang, N. Wu, Y. Tang, *Adv. Energy Mater.* **2017**, *7*, 1700920; b) J. Zhu, Y. Li, B. Yang, L. Liu, J. Li, X. Yan, D. He, *Small* **2018**, *14*, 1801836; c) L. Fan, Q. Liu, S. Chen, K. Lin, Z. Xu, B. Lu, *Small* **2017**, *13*, 1701011; d) A. Yu, Q. Pan, M. Zhang, D. Xie, Y. Tang, *Adv. Funct. Mater.* **2020**, *30*, 2001440.

[23] a) T. Deng, X. L. Fan, C. Luo, J. Chen, L. Chen, S. Hou, N. Eidson, X. Q. Zhou, C. S. Wang, *Nano Lett.* **2018**, *18*, 1522–1529; b) C. L. Liu, S. H. Luo, H. B. Huang, Z. Y. Wang, A. M. Hao, Y. C. Zhai, Z. W. Wang, *Electrochem. Commun.* **2017**, *82*, 150–154; c) C. Vaalma, G. A. Giffin, D. Buchholz, S. Passerini, *J. Electrochem. Soc.* **2016**, *163*, A1295–A1299; d) X. P. Wang, X. M. Xu, C. J. Niu, J. S. Meng, M. Huang, X. Liu, Z. Liu, L. Q. Mai, *Nano Lett.* **2017**, *17*, 544–550.

[24] a) C. L. Zhang, Y. Xu, M. Zhou, L. Y. Liang, H. S. Dong, M. H. Wu, Y. Yang, Y. Lei, *Adv. Funct. Mater.* **2017**, *27*, 1604307; b) A. Eftekhari, *J. Power Sources* **2004**, *126*, 221–228; c) X. F. Bie, K. Kubota, T. Hosaka, K. Chihara, S. Komaba, *J. Mater. Chem. A* **2017**, *5*, 4325–4330; d) X. Jiang, T. R. Zhang, L. Q. Yang, G. C. Li, J. Y. Lee, *ChemElectroChem* **2017**, *4*, 2237–2242.

[25] a) V. A. Nikitina, S. M. Kuzovchikov, S. S. Fedotov, N. R. Khasanova, A. M. Abakumov, E. V. Antipov, *Electrochim. Acta* **2017**, *258*, 814–824; b) T. Hosaka, K. Shimamura, K. Kubota, S. Komaba, *Chem. Rec.* **2019**, *19*, 735–745; c) N. Recham, G. Rousse, M. T. Sougrati, J. N. Chotard, C. Frayret, S. Mariyappan, B. C. Melot, J. C. Jumas, J. M. Tarascon, *Chem. Mater.* **2012**, *24*, 4363–4370; d) K. Chihara, A. Katogi, K. Kubota, S. Komaba, *Chem. Commun.* **2017**, *53*, 5208–5211.

[26] a) Y. N. Chen, W. Luo, M. Carter, L. H. Zhou, J. Q. Dai, K. Fu, S. Lacey, T. Li, J. Y. Wan, X. G. Han, Y. P. Bao, L. B. Hu, *Nano Energy* **2015**, *18*, 205–211; b) Z. L. Jian, Y. L. Liang, I. A. Rodriguez-Perez, Y. Yao, X. L. Ji, *Electrochem. Commun.* **2016**, *71*, 5–8; c) J. Zhao, J. X. Yang, P. F. Sun, Y. H. Xu, *Electrochem. Commun.* **2018**, *86*, 34–37.

[27] a) R. J. C. Dubey, J. Nussli, L. Piveteau, K. V. Kravchyk, M. D. Rossell, M. Campanini, R. Erni, M. V. Kovalenko, N. P. Stadie, *ACS Appl. Mater. Interfaces* **2019**, *11*, 17686–17696; b) J. H. Lang, J. R. Li, X. W. Ou, F. Zhang, K. S. Shin, Y. B. Tang, *ACS Appl. Mater. Interfaces* **2020**, *12*, 2424–2431; c) H. C. Gao, L. G. Xue, S. Xin, J. B. Goodenough, *Angew. Chem. Int. Ed.* **2018**, *57*, 5449–5453; *Angew. Chem.* **2018**, *130*, 5547–5551.